






# Channel Performance Metrics and Evaluation for XR Head-Mounted Displays with mmWave Arrays

Alexander Marinšek , *Student Member, IEEE*, Xuesong Cai , *Senior Member, IEEE*,  
Lieven De Strycker , *Member, IEEE*, Fredrik Tufvesson , *Fellow, IEEE*, Liesbet Van der Perre , *Senior Member, IEEE*

**Abstract**—Millimeter-wave (mmWave) technology holds the potential to revolutionize head-mounted displays (HMDs) by enabling high-speed wireless communication with nearby processing nodes, where complex video rendering can take place. However, the sparse angular profile of mmWave channels, coupled with the narrow field of view (FoV) of patch-antenna arrays and frequent HMD rotation, can lead to poor performance.

We introduce six channel performance metrics to evaluate the performance of an HMD equipped with mmWave arrays. We analyze the metrics using analytical models, discuss their impact for the application, and apply them to 28 GHz channel sounding data, collected in a conference room using eight HMD patch-antenna arrays, offset by 45° from each other in azimuth.

Our findings confirm that a single array performs poorly due to the narrow FoV, and featuring multiple arrays along the HMD's azimuth is required. Namely, the broader FoV stabilizes channel gain during HMD rotation, lessens the attenuation caused by line of sight (LoS) obstruction, and increases the channel's spatial multiplexing capability. In light of our findings, we conclude that it is imperative to either equip the HMD with multiple arrays or, as an alternative approach, incorporate macroscopic diversity by leveraging distributed access point (AP) infrastructure.

**Keywords**—Extended reality, wireless, millimeter-wave, antenna configuration, channel measurements

## I. INTRODUCTION

A head-mounted display (HMD) is a wearable piece of equipment that projects high-fidelity visuals in front of the user's eyes. Rendering video on a nearby computer or edge processing node can reduce HMD hardware complexity and aid ergonomics [1]. Millimeter-wave (mmWave) technology can provide the multi-Gbps data rates required for extended reality (XR) content streaming, owing to the ample bandwidth availability in the mmWave spectrum (30–300 GHz) [2–4]. To overcome large-scale fading, mmWave transceivers feature directive antenna arrays. These augment the transceiver's gain to combat path loss and shadowing, while simultaneously mitigating the effects of small-scale and frequency-selective fading [5]. However, mmWave channels are known for their sparsity. That is, they feature few powerful signal components. This begs the question: *how many antenna arrays* should an HMD have, and what are the *relevant channel performance metrics* for XR applications?

A. Marinšek, L. De Strycker, and L. Van der Perre are with ESAT-WaveCore, KU Leuven, Ghent, Belgium. X. Cai and F. Tufvesson are with LTH-EIT, Lund University, Lund, Sweden. Email of the corresponding authors: {alexander.marinsek, liesbet.vanderperre}@kuleuven.be

MmWave channels are characterized by sparse multipath profiles. Analyses of channel measurement data, collected in office and conference room environments, show that mmWave channels seldom feature more than five multipath component (MPC) clusters, among which only a few have sufficient gain and capturing the line of sight (LoS) cluster is often essential for sustaining high-throughput applications [6–10]. Hence, placing a patch-antenna array with a  $-3$  dB field of view (FoV) of 90° in such a channel and having it continuously rotate on the head of an XR user is akin to poor signal reception.

In recent years, researchers have been investigating signal reception quality in the context of mmWave 5G NR mobile networks, and they have identified several adverse circumstances associated with handheld devices. These include movement, orientation changes, obstruction by objects, and physical contact between the device's antennas and the user. For instance, simply walking 15 m along a corridor can lead to a degradation of signal strength by approximately 15–20 dB, with additional fluctuations of around  $\pm 15$  dB depending on the specific user [11]. Changing the smartphone's orientation from vertical to horizontal can result in a halving of performance, as noted in [12], which observed a 50% decrease in data rate in an IEEE 802.11ad network. Moreover, shadowing from the user's body can attenuate the signal by 20–25 dB in various handheld use cases [13, 14]. Even holding the smartphone in one's palm can absorb up to 15 dB of signal strength, while a mere finger interacting with the device can cause a 3 dB disruption to the mmWave link [15, 16]. All these factors pose possible challenges to mmWave communications systems in XR HMDs.

Previous studies on mmWave channel measurements and channel modeling for HMDs have shown that high data rates can be achieved in cluttered indoor environments even with limited signal bandwidth [17, 18], and that a single mmWave antenna array is likely insufficient [19]. Moreover, recent research advocates mmWave-based sensing for complementing and even substituting the HMD's visual tracking systems [20, 21]. Although prior art clearly outlines the potential and challenges associated with mmWave technology for HMDs, there is a lack of insight into how broadening the HMD's FoV by employing multiple antenna arrays can alleviate the channel adversities that occur during HMD rotation.

The work at hand conducts statistical and temporal characterization of mmWave channel gain and capacity for multi-array HMDs. Channel sounding data from a tailor-made 28 GHz measurement campaign is analyzed in order to assess the performance of different mmWave array configurations on

arXiv:2404.19297v1 [eess.SP] 30 Apr 2024

© 2024 IEEE. Personal use of this material is permitted. Permission from IEEE must be obtained for all other uses, in any current or future media, including reprinting/republishing this material for advertising or promotional purposes, creating new collective works, for resale or redistribution to servers or lists, or reuse of any copyrighted component of this work in other works.

This is the accepted version of the published paper with DOI: [10.1109/TCOMM.2024.3392805](https://doi.org/10.1109/TCOMM.2024.3392805)

The measurement data is accessible at <https://zenodo.org/records/10822725>

the HMD. Furthermore, we compare the results against analytical models and discuss their application-level significance. Our contributions are summarized as follows:

- Derivation of six performance metrics, used for assessing the channel of a multi-array HMD, including their analysis using analytical models and a discussion of their application-level significance,
- Analysis of the channel's performance in terms of the derived performance metrics for an HMD employing 1–4 mmWave patch-antenna arrays, and
- Evaluation of additional degrees of freedom, namely, the usage of a rear-HMD headband for array placement, the deactivation of parts of the antenna arrays, and alternative access point (AP) placement possibilities.

We first describe the measurement campaign and post-processing procedures in Section II. Then, we introduce the six performance metrics in Section III and describe the analysis steps in Section IV. In Section V, we report on the performance of configurations featuring 1–4 arrays. In Section VI we evaluate the effects of using a rear headband, altering the number of active HMD antennas, and changing the AP's position. We summarize the main findings while providing an outlook for future research in Section VII. Note that the paper at hand is an extension of our prior work, where we evaluated three of the six performance metrics [22].

*Notation and terminology:*  $\|\cdot\|_F$  is the Frobenius norm,  $\mathbb{E}[\cdot]$  is the expectation operator,  $e$  is the Euler number, and  $(\cdot)^T$  is the matrix transpose. The term *gain* refers to the *power gain* of the wireless channel, consisting of the combined channel and antenna response.

## II. MEASUREMENT SETUP AND POST-PROCESSING

This section outlines the utilized channel sounder, the measurement environment and procedures, as well as the employed channel reconstruction and normalization techniques.

### A. Measurement equipment

Fig. 1 shows the employed switched array multiple-input multiple-output (MIMO) channel sounder, jointly developed by Lund University and Sony. This sounder operates at 28 GHz, has a bandwidth of 768 MHz (1.3 ns time-delay resolution), and utilizes a Zadoff-Chu waveform. The user equipment (UE), which we will refer to as the HMD, consists of 8 planar patch-antenna arrays, offset by  $45^\circ$  from each other in azimuth and featuring  $4 \times 4$  antennas each. Throughout the measurement process, all 8 arrays are continuously sampled, and the channel matrices of specific arrays are extracted during the analysis stage in order to examine the channel performance of various HMD array configurations. The HMD arrays are marked by Roman numerals and VII represents the forward-facing array, as shown in Fig. 1. The small array size (approximately  $2 \times 2$  cm), makes it possible to mount eight arrays to an HMD's plastic frame or headband. Moreover, the arrays would halve in size for the 60 GHz frequency band, and they would become even smaller in the sub-THz spectrum. We foresee that arrays

II and IV are the most critical, as these should not be placed behind the ears in order to avoid obstruction. The ears could otherwise constitute several dB of attenuation, similar to how fingers obstruct the mmWave links on a smartphone [15]. Dry thick hair is less of a problem with an attenuation of about  $0.2 \text{ dB cm}^{-1}$  (e.g., the cross-section of a ponytail) [23].

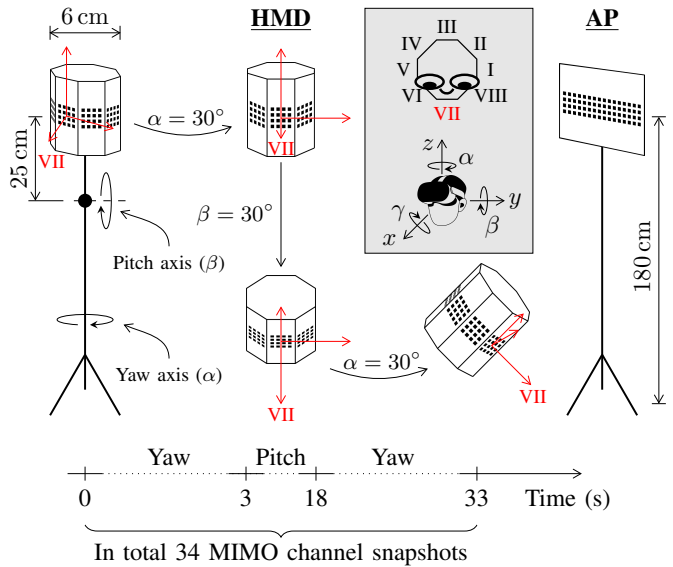


**Fig. 1:** HMD and AP illustration, including the HMD's mobility pattern. HMD array numbering and the extrinsic Euler rotation axes are shown in the gray rectangle. Positive rotations are obtained using the right-hand rule. Array VII points forwards (the same direction as the user's eyes and nose).

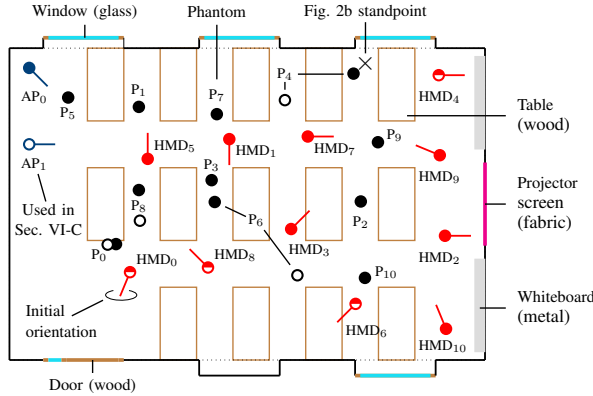
The AP-side is equipped with a single  $16 \times 4$  planar array. All antenna elements on both the HMD and AP are dual-polarized, resulting in a  $256 \times 128$  channel matrix. Sampling is conducted at a rate of  $18.3 \mu\text{s}$  per antenna element combination, which includes averaging over four sounding sequences to reduce measurement noise. The channel snapshot sampling rate is set to 1 Hz, providing sufficient time for sampling all antenna element pairs and for memory writing. Accurate synchronization is achieved by employing rubidium atomic clocks and additional preambles in the sounding waveform. More details on the channel sounder can be found in [24, 25]. The system parameters are listed in Table I.

**TABLE I:** System parameters.

Parameter	Value
Carrier frequency	28 GHz
Sounding signal bandwidth	768 MHz
Time delay resolution	1.3 ns
Largest observable time delay	$2.7 \mu\text{s}$
Individual channel sampling time	$18.3 \mu\text{s}$
Channel snapshot sampling frequency	1 Hz
Measurement duration at each HMD position	33 s
AP array size	$4 \times 16$
HMD array size	$4 \times 4$
Number of HMD arrays	8
Channel snapshot size	$256 \times 128 \times 2048$

## B. Measurement environment

Measurements were conducted at 11 fixed random positions in a conference room, as illustrated in Fig. 2. For each position, the initial orientation of the HMD was randomly chosen (indicated by the red line in Fig. 2a). This initial orientation served as the starting point for the subsequent mobility pattern. Channel sounding was repeated at each position to simulate obstructed LoS (LoS) conditions, where a pre-characterised<sup>1</sup> fiberglass water-filled human phantom was used to obstruct the LoS [26]. The environment remained quasi-static during channel sounding, except for the mobility of the HMD, which will be discussed in the upcoming subsection.



(a) Floor plan. Blue, red, and black markers represent the AP, HMD, and phantom, respectively. Filled and half-filled HMD and phantom markers were considered for AP<sub>0</sub>, while empty (white) and half-empty markers were evaluated for AP<sub>1</sub> (used in Section VI-C). Brown, cyan, gray, and magenta mark tables and the door, windows, metal whiteboards, and a projector screen, respectively. The room size is 6 × 9.15 m.



(b) Setup for position HMD<sub>6</sub> in OLoS conditions.

**Fig. 2:** Conference room measurement environment.

## C. Mobility pattern

We have devised a mobility pattern for the HMD that aims to capture mmWave channel information during directive antenna array rotation. As Fig. 1 shows, the HMD starts in an upright position and is first rotated by 30° in yaw (azimuth). This is

<sup>1</sup>Before the experiment, we evaluated the attenuation of the phantom as well as that of six volunteers by placing the AP and HMD 3 m apart and positioning the obstructing subject in the center of the LoS. The results from a laboratory environment showed a mean attenuation of 12.8 dB for the phantom and 11.8 ± 2.1 dB (mean and standard deviation) for the volunteers.

followed by a 30° downward-pitching movement (elevation, equivalent to leaning forward), and concluded by a final 30° yaw change. Rotation is executed manually using a tripod, to which the HMD is mounted. The forward-tilted HMD is rotated around the tripod's vertical axis during the final yaw rotation. This mimics a person looking down and rotating their entire body by 30° in yaw (leftward rotation).

To ensure precise channel state information during rotation, we maintain angular velocity below 10° s<sup>-1</sup> and tangential velocity below 1 cm s<sup>-1</sup>. Executing a single mobility sequence takes approximately 33 s. The first yaw rotation around the tripod's vertical axis takes 3 s, while the subsequent pitch and the final yaw rotation each take 15 s. The duration is longer for the second yaw rotation, since the HMD covers a longer trajectory when it is tilted down, significantly increasing the radius of the movement. The 25 cm distance between the pitch axis of the tripod and the HMD's center of mass closely reflects the separation between the human cervical vertebrae and the head [27], making the mobility pattern a good representation of XR user head movement. As noted in literature [28–30], roll rotation is far less pronounced than yaw and pitch rotation, therefore, we did not include roll in the mobility pattern.

## D. Signal model and MPC parameter estimation

The channel transfer function (CTF) for the  $m^{\text{th}}$  HMD and the  $n^{\text{th}}$  AP antenna is represented by a superposition of specular MPCs (plane waves since the Fraunhofer distance is < 1 m). The CTF at the  $k^{\text{th}}$  tone (frequency  $f_k$ ) is modelled as

$$\begin{aligned} \mathbf{H}_{m,n}[p, s, i, k] &= \sum_{l=0}^{L-1} \mathbf{g}_{R,m}^T(\phi_{R,l}, \theta_{R,l}, f_k) \begin{bmatrix} \gamma_{HH,l} & \gamma_{HV,l} \\ \gamma_{VH,l} & \gamma_{VV,l} \end{bmatrix} \mathbf{g}_{T,n}(\phi_{T,l}, \theta_{T,l}, f_k) \\ &\times \mathbf{g}(f_k) e^{-j2\pi f_k \tau_l} e^{j2\pi \nu_l t_{m,n}} + \mathcal{N}_{m,n}(f_k), \end{aligned} \quad (1)$$

where indexes  $p$ ,  $s$ ,  $i$ , and  $k$  represent the HMD position, scenario (LoS/OLoS), snapshot index, and sounding tone index (see Table II for a summary of indexes). Values  $\mathbf{g}_{R,m} \in \mathbb{C}^{2 \times 1}$  and  $\mathbf{g}_{T,n} \in \mathbb{C}^{2 \times 1}$  represent the frequency-dependent polarimetric responses of the  $m^{\text{th}}$  HMD (Receiver) and the  $n^{\text{th}}$  AP (Transmitter) antenna, respectively. These further depend on the  $l^{\text{th}}$  MPC's azimuth and elevation of arrival/departure, denoted by  $\phi_{R/T,l}$  and  $\theta_{R/T,l}$ , correspondingly. Note that  $(\cdot)^T$  is the matrix transpose. The parameters  $\gamma_{HH,l}$ ,  $\gamma_{HV,l}$ ,  $\gamma_{VH,l}$ , and  $\gamma_{VV,l}$  represent the horizontal-to-horizontal, horizontal-to-vertical, vertical-to-horizontal, and vertical-to-vertical polarization amplitude gains of the  $l^{\text{th}}$  MPC. Furthermore,  $\mathbf{g}(f_k)$  represents the sounder's system response without antenna arrays,  $\tau_l$  and  $\nu_l$  are the  $l^{\text{th}}$  MPC's time delay and Doppler frequency, respectively,  $t_{m,n}$  is the sampling time, and  $\mathcal{N}$  is white Gaussian noise. Note that  $\mathbf{H}_{m,n}$  is the Fourier transform of the channel impulse response (CIR), represented by  $h_{m,n}$ .

We employ the space alternating generalized expectation-maximization (SAGE) algorithm for estimating the channel's signal components and reconstructing a noiseless channel. While there is no reminiscent noise in the reconstructed



**TABLE II:** Index overview.

Index	Meaning	Index	Meaning
p	HMD position	q	HMD array
s	LoS/OLoS Scenario	m	HMD antenna element
i	Channel snapshot	n	AP antenna element
k	Sounding tone	j	Autocorrelation delay
l	MPC (signal component)	r	Eigenmode (sp. stream)

channel, the estimation accuracy is subject to the ratio between channel gain after beamforming and the noise floor. This signal-to-noise ratio (SNR) is around 50 dB across the measured channel snapshots. The corresponding error in the estimated channel parameters (Cramér-Rao lower bound) is approximately inversely proportional to the aforementioned SNR after beamforming [31]. The reconstructed channel allows us to compare individual gains with higher accuracy and to later analyze channel capacity at different SNRs.

### E. Channel normalization

For calculating the channel capacity, we apply channel normalization since removing large-scale fading allows us to study capacity as a function of the SNR. This is done in order to solely assess the effects of limited FoV and the benefits of broadening the FoV by introducing additional antenna arrays. Normalized channel matrices are derived as follows

$$\mathbf{H}_Q[p, s, i, k] = \frac{MN IK}{\sqrt{\sum_{i=0}^{I-1} \sum_{k=0}^{K-1} \|\mathbf{H}_s^{\text{rec}}[p, s, i, k]\|_{\text{F}}^2}} \mathbf{H}_Q^{\text{rec}}[p, s, i, k], \quad (2)$$

where  $\mathbf{H}_Q^{\text{rec}}$  is the reconstructed channel matrix for a  $Q$ -array system without normalization and  $\|\cdot\|_{\text{F}}^2$  is the square of the Frobenius norm. Values  $M = 256$  and  $N = 128$  are the number of HMD and AP antenna ports, respectively, while  $I = 34$  and  $K = 2048$  represent the number of snapshots and sounding tones, correspondingly. The resulting mean channel gain over the frequency band becomes  $E[\sum_{k=0}^{K-1} |\mathbf{H}_{m,n}[p, s, i, k]|^2] = 1$ . We conduct normalization on the full  $256 \times 128$  channel matrices (employing all 8 HMD arrays), after which we extract the sub-channels, corresponding to the studied HMD antenna array configurations, in order to preserve their gain ratios for further evaluation. Note that this only applies to the spatial multiplexing capability and minimal service performance metrics, described in Section III-E and Section III-F, respectively. The preceding four gain-based metrics evaluate the non-normalized channel, i.e.,  $\mathbf{H}^{\text{rec}}$ .

Below is an example showing a full channel matrix and the sub-channels of a single-array configuration (discussed in Section IV). Indexes  $p, s, i$ , and  $k$  are omitted for clarity.

$$\mathbf{H} = \begin{bmatrix} \mathbf{H}_{1,1} & \cdots & \mathbf{H}_{1,N} \\ \vdots & \ddots & \vdots \\ \mathbf{H}_{193,1} & \cdots & \mathbf{H}_{193,N} \\ \vdots & \ddots & \vdots \\ \mathbf{H}_{224,1} & \cdots & \mathbf{H}_{224,N} \\ \vdots & \ddots & \vdots \\ \mathbf{H}_{M,1} & \cdots & \mathbf{H}_{M,N} \end{bmatrix} \quad (3)$$

**H<sub>1</sub>**  
Channel matrix of a  
single-array HMD  
(array VII)

## III. PERFORMANCE METRICS

This section describes the below six performance metrics. For each, we conduct an initial study based on analytical models, mathematically formulate the metric, and conclude with its application-level relevance. Per sub-section, the metrics are:

- A. Gain dependency on the azimuth FoV,
- B. Gain stability during rotation,
- C. Attenuation due to LoS obstruction,
- D. Delay dispersion and frequency-selective fading,
- E. Spatial multiplexing capability, and
- F. Minimal service.

### A. Gain dependency on the azimuth FoV

We first describe the *power gain* (referred to as *gain*) due to a signal component that impinges on an HMD, equipped with multiple patch-antenna arrays along its azimuth. To illustrate the relevance of the metric, we employ a theoretical analysis that assumes the antennas have no coupling between them and that they feature ideal responses with a  $-3$  dB FoV of  $90^\circ$ . We express the compound gain as a superposition of the gains recorded by individual antennas on each of the arrays as

$$\eta_Q(\alpha, \phi) = NM_Q \sum_{q=0}^{Q-1} |\alpha|^2 \cos^2\left(\phi - q \frac{2\pi}{Q}\right) \left| \left| \frac{|\phi - q \frac{2\pi}{Q}|}{\pi} \right| - 2 \right|, \quad (4)$$

where  $|\alpha|^2$  and  $\phi$  are the gain and azimuth angle of the impinging signal component, while  $Q$  represents the number of employed HMD arrays, each consisting of  $M_Q$  antennas. The impinging angle relative to each array's boresight is determined by  $\phi - q \frac{2\pi}{Q}$ , while the last term in Equation (4) limits the radiation pattern to  $\pm \frac{\pi}{2}$ . We see that reducing the number of arrays ( $Q$ ) does not necessarily decrease the compound gain by a factor of  $Q$  if the channel's MPCs are unequally distributed along the azimuth. For example, a single-array configuration might receive similar gain to a 4-array configuration when oriented towards the LoS. However, orienting the single-array configuration's narrow FoV away from the channel's major MPCs would result in a far lower gain than suggested merely by the reduction in array gain. To evaluate the effects of a limited compound HMD FoV on the gain for the empirical data, we derive the gain ratio between a  $Q$ -array and a full 8-array configuration. Considering all MPCs per channel snapshots, we drop parameters  $\alpha$  and  $\phi$  to derive the ratio as

$$\overline{\Delta\eta_Q}[p, s, i] = \frac{\overline{\eta_Q}[p, s, i]}{\overline{\eta_8}[p, s, i]}, \quad (5)$$

where  $\overline{\eta_Q}[p, s, i]$  is the mean power gain recorded by a  $Q$ -array HMD across the 768 MHz bandwidth. If the  $Q$ -array configuration is illuminated by the LoS, then the metric yields  $\overline{\Delta\eta_Q} \geq \frac{Q}{8}$  since only a few of the eight arrays of the full configuration can capture the LoS simultaneously. The result becomes  $\overline{\Delta\eta_Q} < \frac{Q}{8}$  if the  $Q$ -array configuration's FoV can not capture the major MPCs, including the LoS.

*Application-level relevance:* An FoV which is too narrow leads to a pronounced reduction in gain. The resulting data rate decrease can ripple through the application layer, reducing XR video quality and possibly causing outage.

### B. Gain stability during rotation

The time dynamics of channel gain during HMD rotation are assessed through gain spread and persistence. We derive these, respectively, by calculating the standard deviation and the autocorrelation of the gain across the HMD orientations (channel snapshots) that make up the mobility pattern. The gain's standard deviation is derived in the logarithmic domain (in decibels) in order to better highlight the relative gain changes, regardless of the mean gain, according to the below

$$\sigma_{\eta,Q}[p, s] = \frac{10}{I} \sqrt{\sum_{i=0}^{I-1} \log_{10}^2 \left( \frac{\overline{\eta_Q}[p, s, i]}{\overline{\eta_Q}[p, s]} \right)} \quad [\text{dB}], \quad (6)$$

where  $\overline{\eta_Q}[p, s] = \mathbb{E}[\overline{\eta_Q}[p, s, i]]$  is the mean gain across all snapshots for a given position-scenario (LoS/OLoS) pair. We calculate the gain's autocorrelation as a normalized value in the range of  $r \in (-1, 1)$  as follows

$$r_{\eta,Q}[p, s, j] = \frac{\sum_{i=0}^{I-j-1} (\overline{\eta_Q}[p, s, i] - \overline{\eta_Q}[p, s]) (\overline{\eta_Q}[p, s, i+j] - \overline{\eta_Q}[p, s])}{\sum_{i=j}^{I-j-1} (\overline{\eta_Q}[p, s, i] - \overline{\eta_Q}[p, s])^2}, \quad (7)$$

where  $j$  represents the delay in terms of channel snapshots.

*Application-level relevance:* A high standard deviation of the gain during the conducted rotation may lead to video resolution adaptation. Moreover, a low autocorrelation shows low gain stability (frequent changes), which may require additional video frame buffering. This leads to higher XR video latency.

### C. Attenuation due to LoS obstruction

LoS obstruction by a person (or phantom) other than the HMD user causes substantial attenuation. We anticipate the latter will conform with the geometrical theory of diffraction (GTD)<sup>2</sup>, which describes attenuation according to the obstructing object's shape and its distance to the AP and HMD [26]. The discrepancy from the GTD, presented alongside the results, will highlight the array configuration's capability of capturing additional unobstructed MPCs. To determine the attenuation upon LoS obstruction, we compare the LoS channel gain against that of the OLoS scenario using

$$\overline{\Delta\eta_Q^{(\text{bl})}}[p, I] = \frac{\sum_{i=0}^{I-1} \overline{\eta_Q}[p, \text{LoS}, i]}{\sum_{i=0}^{I-1} \overline{\eta_Q}[p, \text{OLoS}, i]}, \quad (8)$$

where the total number of evaluated snapshots  $I$  is in this assessment limited to either one or all available snapshots. We

first evaluate for  $I = 1$  which gives us a comparison of the channel gain of the first snapshot at each position. This is done since at the start of each measurement, the HMD part of the channel sounder is approximately in the same position and orientation for both the LoS and OLoS scenario. The orientation of the HMD can vary during subsequent snapshots due to the manual execution of the mobility sequence. In the second step of the assessment,  $I$  is increased to incorporate all available snapshots per position and scenario. This results in a comparison of the mean gain during LoS and OLoS conditions.

*Application-level relevance:* LoS obstruction by another person's head or body can cause substantial attenuation. This metric shows how severe the attenuation is and whether the HMD can benefit from receiving other unobstructed MPCs.

### D. RMS delay spread and frequency-selective fading

A reflective environment can lead to the transmitted signal arriving at the receiver at multiple instances in time due to multipath propagation. Its extent can be summarized using the root mean square (RMS) delay spread, calculated as follows

$$\sigma_{\tau,Q}[p, s, i] = \sqrt{\frac{\sum_{u=0}^{U-1} \|\mathbf{h}_Q[u]\|_{\text{F}}^2 \tau[u]^2}{\sum_{u=0}^{U-1} \|\mathbf{h}_Q[u]\|_{\text{F}}^2} - \left( \frac{\sum_{u=0}^{U-1} \|\mathbf{h}_Q[u]\|_{\text{F}}^2 \tau[u]}{\sum_{u=0}^{U-1} \|\mathbf{h}_Q[u]\|_{\text{F}}^2} \right)^2}, \quad (9)$$

where  $\|\mathbf{h}_Q[u]\|_{\text{F}}^2$  is the power delay profile (PDP) of a  $Q$ -array HMD and  $\tau[u]$  is the time delay of the  $u^{\text{th}}$  CIR sample. The corresponding coherence bandwidth is approximately inversely proportional to the channel's RMS delay spread [33]. When the transmission bandwidth is wider than the coherence bandwidth, frequency-selective fading occurs. Its severity is assessed through the gain's persistence over the measured bandwidth, calculated as follows

$$\xi_Q[p, s, i] = \frac{\sum_{k=0}^{K-1} (\eta_Q[p, s, i, k] - \overline{\eta_Q}[p, s, i])^2}{\overline{\eta_Q}[p, s, i]^2}. \quad (10)$$

Recall that  $\eta_Q$  is the gain of the compound MIMO channel across multiple AP-HMD antenna pairs. The intuition behind the metric is that the ratio between the gain's standard deviation and its mean across the transmission bandwidth reduces as more channels are included. For ideally persistent gain across the measured bandwidth (flat fading),  $\xi$  would reduce to zero.

*Application-level relevance:* The RMS delay spread indicates the coherence bandwidth within which roughly flat fading is expected. This highlights the needed complexity of the channel equalization with regards to the employed transmission bandwidth. The latter depends on the required data rate.

### E. Spatial multiplexing capability

Transmission can take place over a single stream, called dominant eigenmode transmission (DET), or over several streams, referred to as spatial multiplexing (SM). The maximal

<sup>2</sup>A detailed description of the GTD can be found in [26] and [32].

number of multiplexed streams is governed by the channel as  $R \leq \min(M, N)$ . SM exploits the channel's rank (orthogonality) to increase channel capacity as follows

$$C_Q[p, s, i] = \max_{\sum \rho_{Q,r} \leq M_Q} \sum_{r=0}^{R_Q-1} \log_2 \left( 1 + \frac{E_s \rho_{Q,r}}{M_Q N_0} \overline{\lambda_{Q,r}} \right), \quad (11)$$

where  $R_Q$  is the rank of channel matrix  $\mathbf{H}_Q$  (number of non-zero eigenmodes),  $\overline{\lambda_{Q,r}}$  is the mean  $r^{\text{th}}$  eigenvalue of  $\mathbf{H}_Q \mathbf{H}_Q^H$ ,  $M_Q$  is the number of channel outputs (HMD antenna ports),  $\frac{E_s}{N_0}$  is the symbol energy over noise spectral density, and the power allocated to the  $r^{\text{th}}$  eigenmode (orthogonal stream) is represented by  $\rho_{Q,r}$  and determined according to the waterfilling algorithm [33]. Capacity is largest for a full-rank channel with equal-gain eigenmodes (unitary channel). A LoS channel may also have a full-rank, however, its gain is often severely unevenly distributed among its eigenmodes [34]. Maximizing capacity according to waterfilling leads us to allocate power to a limited number of streams in such a channel, whereas power would be equally distributed among the eigenmodes of a unitary channel. To evaluate the SM capabilities of the considered array configurations and to assess the profitability of allocating power to more than one stream, we progressively increment the number of employed streams ( $R_Q$ ) in Equation (11) and observe the obtained capacity. Note that  $R_Q = 1$  reduces Equation (11) to DET, equivalent to joint maximum-ratio transmission and combining (MRT/MRC).

*Application-level relevance:* Multiplexing several streams can increase the data rate and enhance XR video quality. Knowing the increase in capacity per additional stream allows HMD designers to appropriately scale the system's complexity and avoid overprovisioning of the hardware.

#### F. Minimal service

The channel capacity derived using Equation (11) also serves as the upper bound of the achievable data rate. Typically, channel characterization studies evaluate the mean and sum (for multi-user scenarios) channel capacity [5]. However, we foresee that for XR applications, where video stream reception represents the main payload, it is more important to study the minimal capacity, since it determines the worst-case video quality. As most use cases, XR applications allow for a limited amount of outage. Namely, video streaming has an approximately 97% reliability requirement, allowing up to 3% of outage [35]. We thus primarily focus on analyzing the capacity's 3<sup>rd</sup> percentile and on evaluating how this value is affected by the number of employed antenna arrays. Moreover, considering channel gain normalization, we study the minimal service's dependency on the receive SNR by varying  $\frac{E_s}{N_0}$ .

Equation (11) employs mean eigenmode gain, averaged across the transmission bandwidth. This is a measure of the potential achievable rate over the full transmission bandwidth. However, individual subcarriers might undergo more pronounced fading. We assess both approaches in order to evaluate whether the same trends in capacity occur when increasing the number of employed arrays. We derive the minimal service

on a per-subcarrier basis (375 kHz spacing) by evaluating the statistics of  $C_Q[p, s, i, k]$ , without eigenmode averaging.

*Application-level relevance:* Channel capacity provides the upper bounds of the data rate, which in terms limits the achievable XR video quality. Since video streaming has a 97% reliability constraint, the capacity's 3<sup>rd</sup> percentile determines the minimal service, that is, the minimal relevant capacity [35].

## IV. ANALYSIS PROCEDURES

This section introduces the analysis procedures, utilizing the performance metrics outlined in the preceding section and applying them to channel measurement data. The following sections describe our approach to:

- A. Evaluating the performance of a multi-array HMD,
- B. Investigating the profitability of a rear-HMD headband,
- C. Assessing performance degradation when activating a limited number of antennas in HMD arrays, and
- D. Exploring the impact of the AP's position on the channel.

#### A. Multi-array HMD performance

The primary focus of the study at hand is to estimate the performance of an HMD, which, in its final design, would feature between 1 and 4 mmWave antenna arrays. This is achieved by applying the proposed performance metrics from Section III to mmWave channel measurements for the antenna array configurations illustrated in Fig. 3. The four configurations are primarily forward-oriented, as we envision that future HMDs will not feature a rear headband in order to prioritize ergonomics and aesthetics. As concluded in our initial analysis [22], there is no clear benefit to including more than 4 antenna arrays, apart from array gain. This is supported by the fact that 4 patch-antenna arrays already provide approximately uniform 360-degree coverage.

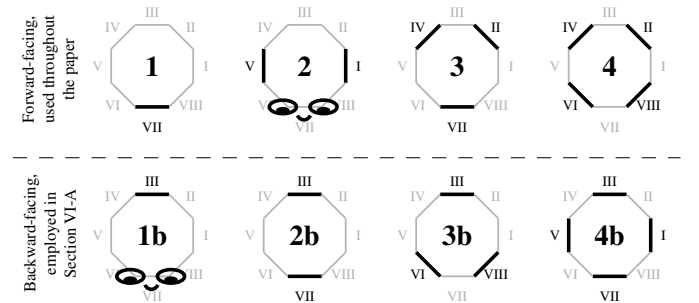


**Fig. 3:** Studied HMD array configurations, top-down view. The top and bottom row show the forward- and backward-facing configurations, respectively.

#### B. Utilizing a rear headband

A considerable number of present-day HMDs incorporate a rear headband. Although this makes the HMD more conspicuous, it does offer additional mounting space for antenna arrays. We evaluate the benefits of featuring a rear HMD headband and utilizing it for array placement by comparing the forward-facing configurations in Fig. 3 with their

backward-facing counterparts. The profitability of the rear headband is established by evaluating the gain ratio as follows

$$\overline{\Delta\eta_Q^{(\text{rh})}}[p, s, i] = \frac{\overline{\eta_Q^{(b)}}[p, s, i]}{\overline{\eta_Q^{(f)}}[p, s, i]}, \quad (12)$$

where  $\overline{\eta_Q^{(f)}}$  and  $\overline{\eta_Q^{(b)}}$  represent the mean gain of a forward- or backward-facing  $Q$ -array configuration, respectively.

### C. Activating a limited number of antennas in HMD arrays

Wireless HMDs are energy-constrained devices, and powering off the radio frequency (RF) chains of individual antennas can reduce their energy consumption. The drawback is a possibly lower spatial diversity gain due to the smaller number of combined signals, which may simultaneously suffer from fading [36]. To evaluate the impact of powering off RF chains, we analyze the channel in terms of the six performance metrics for an HMD that utilizes 1–16 antennas per array, as shown in Fig. 4. We conduct the analysis by selecting the same antennas on all HMD arrays (e.g., the same row on all  $Q$ -arrays for  $1 \times 4$ ) and evaluating their corresponding channel matrix. We analyze only the 3-array configuration, which showed prosperous performance when using all 16 antennas per array, as reported later in Section V. We repeat the evaluation for all possible sub-array positions and report the joint results. For instance, we examine four different  $1 \times 4$  sub-arrays, corresponding to the four rows in the  $4 \times 4$  array. The results in Section VI-B show the joint statistical distributions. We employ rectangular sub-arrays with equidistant antenna spacing in order to also assess the differences between vertical and horizontal shapes.

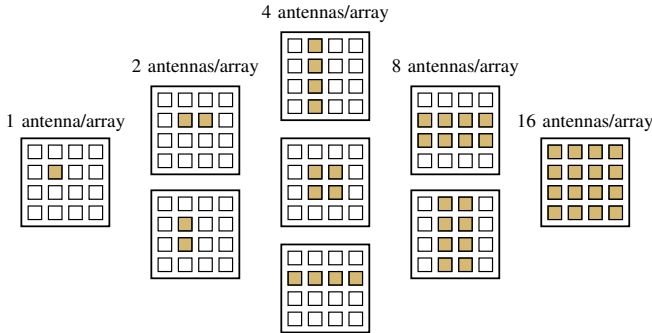


**Fig. 4:** Examples of the evaluated rectangular HMD antenna sub-array shapes (active antennas are marked yellow). For each sub-array, all possible locations within the full  $4 \times 4$  array are included in the analysis.

In addition to the six performance metrics, we assess the dependency of channel gain correlation on the number of active HMD antennas, providing a measure of how likely the channels are to simultaneously suffer from fading. First, we derive the channel gain covariance matrix as per [37] as

$$\mathbf{R}[p, s, i] = \frac{1}{K} \sum_{k=0}^{K-1} |\text{vec}(\hat{\mathbf{H}}_{\text{rec}}[p, s, i, k])|^2 |\text{vec}(\hat{\mathbf{H}}_{\text{rec}}[p, s, i, k])^H|^2, \quad (13)$$

where  $\text{vec}(\hat{\mathbf{H}}_{\text{rec}}[p, s, i, k])$  is the recorded sub-channel matrix at the  $k^{\text{th}}$  sounding tone, reorganized from an  $\hat{M} \times \hat{N}$  matrix

into an  $\hat{M}\hat{N} \times 1$  vector. Equation (13) thus derives the gain covariance among channels by multiplying the channel gains of each combination of two channels at every sounding tone. We normalize the covariance matrix and calculate its mean to obtain the mean channel gain correlation per channel snapshot. The decrease in correlation, observed with the use of additional antennas (from 1 to 16), shows the dependency of spatial diversity on the number of active RF chains.

### D. Impact of AP position and path loss assessment

The position of the AP plays an important role in optimizing signal coverage and enhancing network performance. For example, a ceiling-mounted AP is less susceptible to blockage, a corner-mounted AP may cover the entire floor area with a single array's FoV, and a wall-mounted AP can utilize additional walls as reflective surfaces. To evaluate the latter two hypotheses, we analyze and compare performance in LoS and OLoS conditions for either a corner-mounted or a wall-mounted AP. To achieve this, we repeat part of the measurements (red-white markers in Fig. 2a) after moving the AP out of the corner and placing it parallel to the nearby wall (blue-white marker in Fig. 2a). We then compare the mean channel gain, the time delay, and the azimuth spread between the two AP deployments to establish the influence of the AP's position on channel performance. The RMS delay spread ( $\sigma_\tau$ ) is calculated according to Equation (9), wherein the subtracted term represents the square of the mean excess delay ( $\bar{\tau}^2$ ). We include the latter in the evaluation to provide an easier comparison between our measurements and the prior art. Azimuth spread is calculated according to [6] as

$$\sigma_\phi = \sqrt{-2 \log_{10} \left( \frac{\sum_{l=0}^{L-1} e^{j\phi_{R,l}} \|\alpha_l\|_{\text{F}}^2}{\sum_{l=0}^{L-1} \|\alpha_l\|_{\text{F}}^2} \right)}, \quad (14)$$

where  $\|\alpha_l\|_{\text{F}}^2$  is the  $l^{\text{th}}$  MPC's combined gain across all polarizations. A large  $\sigma_\phi$  signifies that the MPCs impinging on the receiver are highly spread out along the azimuth. Note that some prior art, such as [38], applies a slightly different notation and the relationship to Equation (14) is  $\sigma_\phi = \sqrt{-\log_{10}(1 - \Lambda^2)}$ , where  $\Lambda$  is the alternative angular spread definition. We opted for Equation (14) due to its ability to assess differences in angular spread at large spread values, where  $\Lambda$  would otherwise quickly converge towards one.

In this context, we also conduct an analysis of the LoS path loss exponent (PLE) to characterise the measurement environment and verify the conformity of our data with the prior art [6, 10, 38, 39]. The PLE is derived by fitting a linear regression line to the gain of the first channel snapshot at each HMD position, while minimizing the mean squared error. The PLE applies to the general path loss equation, noted below

$$\text{PL}(f, d) = \text{PL}(f, d_0) \cdot \left( \frac{d}{d_0} \right)^n \cdot \mathcal{X}_\sigma, \quad (15)$$

where  $n$  is the PLE,  $\text{PL}(f, d_0)$  is the path loss at a reference distance  $d_0$ , and  $\mathcal{X}_\sigma$  represents shadow fading ( $\mathcal{X}_\sigma \geq 1$ ).

**TABLE III:** Overview of the employed performance metrics and the main insight for mmWave HMDs. The column *Sec.* lists the sections that contain the results corresponding to the described performance metrics.

Metric	Sec.	Description	Insight for mmWave HMDs
Gain dependency on the azimuth field of view	V-A	Reduction in gain, relative to a full $360^\circ$ azimuth FoV. Low values indicate that the configuration can not capture the dominant MPCs.	A single planar HMD array can not capture sufficient MPCs. Multiple HMD arrays or distributed APs are required.
Gain stability during rotation	V-B	The gain's standard deviation and autocorrelation during rotation. Small std. deviation and high autocorrelation indicate good stability.	Already two arrays reduce gain fluctuation, while adding more arrays further decreases gain spread with diminishing returns.
Attenuation due to LoS obstruction	V-C	Attenuation due to a person obstructing the LoS. Lower values show that the configuration can benefit from alternative propagation paths.	The HMD requires a large enough compound FoV to capture alternative MPCs when the LoS becomes obstructed.
RMS delay spread and frequency-selective fading	V-D	A measure of the MPC time delay differences and the severity of fading dips across the transmission bandwidth (ideally zero).	Configurations with different FoVs all experience a similar RMS delay spread, requiring similar channel equalization complexity.
Spatial multiplexing capability	V-E	The capability of the array configuration to benefit from spatial multiplexing. The higher the capacity per additional stream, the better.	All except the single-array configuration (insufficient FoV) show significant capacity improvement due to spatial multiplexing.
Minimal service	V-F	The minimal achievable channel capacity. Larger values indicate higher potential data rates, hence, better video quality.	A sufficient FoV (metric V-A) is essential for high single-stream capacity. Additional arrays can enhance multi-stream capacity.

## V. INFLUENCE OF ANTENNA ARRAY CONFIGURATION

This section applies the proposed performance metrics to channel measurements in order to approximate the performance of an HMD featuring a variable number of antenna arrays. All metrics from Section III are employed to show the trade-offs in utilizing less antenna arrays than what would result in  $360^\circ$  azimuth coverage. We focus on the full channel gain and minimum/mean service performance for both spatial multiplexing (SM) and dominant eigenmode transmission (DET). We consider full  $4 \times 4$  HMD antenna arrays and the  $AP_0$  deployment for the purpose of the current study step. All gain and ratio values are from hereon presented on a logarithmic scale (in dB). Table III provides a summary of the metrics and the insights they provide for mmWave HMDs.

### A. Gain dependency on the azimuth FoV

Fig. 5 shows (from right to left) that deactivating half of the HMD arrays, i.e., using four arrays, results in a gain loss proportional to the reduction in array gain (red line). A similar observation holds for a 3-array configuration. The median gain for a 2-array configuration decreases noticeably more than the array gain, indicating an insufficiently wide FoV. This becomes even more apparent for the single-array configuration. The highly-negative values for the single- and 2-array configuration were recorded when the LoS and the major MPCs did not fall within the configuration's azimuth FoV due to HMD rotation.

These observations contradict the DET gain results from our preceding work [22], where the reduction in median DET gain ( $\times$  mark in Fig. 5) is lesser than the reduction in array gain (red line). In the DET results, the benefits of a 4<sup>th</sup> array are also far less pronounced. We associate this with the fact that, in the presence of a LoS component, DET beams primarily towards the LoS, hence reducing the advantages of a multi-array system. Lastly, from the blue boxes, we notice a single-array HMD performs better when standing upright than when tilted down, while the other configurations exhibit similar performance throughout the mobility sequence. This is due to the single array not receiving many prosperous MPCs when angled down since the floor is covered with a carpet and

often cluttered (table and chair legs). The latter also holds for DET gain, as demonstrated in our previous work [22].

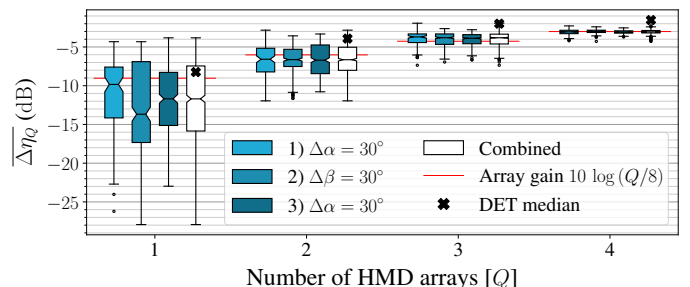


**Fig. 5:** Gain ratio per mobility sequence part (blue) and combined (white). The middle line is the median ( $P_{50}$ ), whiskers show  $P_{50} \pm 1.5(P_{75} - P_{25})$ , dots mark outliers, while notches show the 95% median confidence interval [40]. The same box plot definition is applied throughout the paper.

### B. Gain stability during rotation

Gain stability during the course of a 33s measurement is assessed in Fig. 6. Standard deviation is used to evaluate the gain's spread, while autocorrelation shows its temporal consistency. The noticeable dispersion of points in Fig. 6a shows that a single-array HMD experiences both high gain spread and low gain consistency. The tails, starting from each point, show how the results change when increasing the autocorrelation delay from one sample ( $j = 1$ ) to five samples ( $j = 5$ ) and reducing the number of gain time series samples over which the standard deviation is computed by  $2j$  (remove first and last  $j$ -samples). For an easier overview and comparison against other array configurations, the mean tails are plotted at the top right of Figs. 6a–6d. As can be seen in Fig. 6b, including a 2<sup>nd</sup> array increases gain consistency; however, the gain spread during the course of a measurement remains high. This is reduced by adding a 3<sup>rd</sup> array, as observed in Fig. 6c. A 4<sup>th</sup> array further decreases gain spread by a small amount, visible by comparing the mean markers (colored white) in Figs. 6c and 6d. Note that gain consistency increases with each additional HMD array in spite of the lower autocorrelation ( $r$  in Fig. 6). The latter originates from a stable gain with slight variation, resembling



a constant value with superimposed noise. Such outliers can be detected by either examining the time series data or by observing the vertical tails in Fig. 6d.

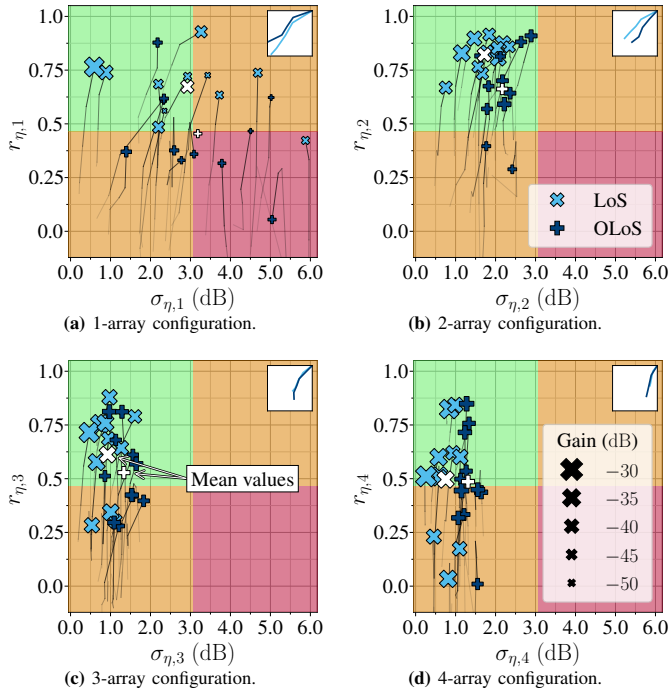


**Fig. 6:** Gain stability for the 11 HMD positions and LoS/OLoS, based on the gain's standard deviation ( $\sigma_Q$ , horizontal) and autocorrelation ( $r_Q$ , vertical). The marker tails represent an increase in delay ( $j$ ) from one to five samples, with the tail averages summarized in the top-right box of each plot.

### C. Attenuation due to LoS obstruction

The adverse effects of LoS obstruction are presented in Fig. 7. Here we focus primarily on positions HMD<sub>5</sub> and HMD<sub>9</sub>, when the HMD was oriented towards the AP (highlighted in red). From the two, we notice that i) the effects of blockage on a single-array HMD are approx. 2 dB more severe than for a 3-array HMD ii) a 3- and 4-array configuration fare similarly in the presence of blockage, and iii) the adverse effects of LoS obstruction noticeably decrease with distance, as the gain loss becomes as low as 5 dB for position HMD<sub>9</sub>. The bottom row in Fig. 7 shows the reference gain loss, derived analytically using the GTD. We consider the obstructing head can be approximated as a vertical cylinder with a 15 cm diameter and that the OLoS passes through the cylinder's central axis. The GTD results confirm the diminishing attenuation with distance trend, and they align well with the results of a single-array configuration when it is oriented towards the AP (positions HMD<sub>5</sub> and HMD<sub>9</sub>). However, we notice that the measured attenuation for a 4-array configuration (full azimuth coverage) is several dB smaller than the GTD suggests. We explain this by the fact that the analytical model does not consider multipath propagation, which can reduce the attenuation caused by blockage. The negative values in Fig. 7 originate from comparisons where the HMD had no clear LoS due to poor orientation (misalignment) in neither the LoS nor

the OLoS scenario. Recall that the orientations of the arrays in the 2-array configuration are orthogonal to the array in a single-array system. As a result, the effects of blockage on a 2-array HMD are more pronounced when the HMD is oriented perpendicular to the AP.

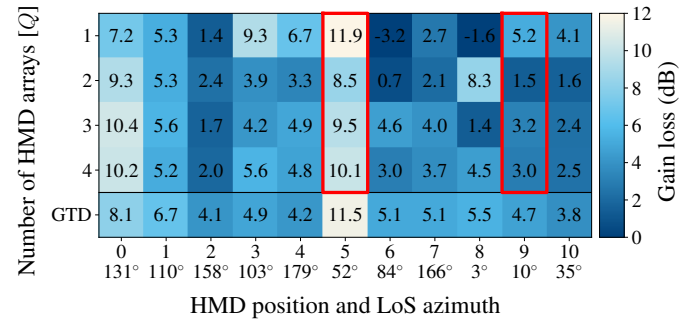


**Fig. 7:** LoS/OLoS ratio for the 1<sup>st</sup> snapshot and the GTD analytical reference. Red shows the positions where the HMD was oriented towards the AP.

Fig. 8 shows the ratio between mean LoS and mean OLoS gain. From it, we can confirm that the 3- and 4-array configurations are similarly affected by blockage. The single-array configuration features on average several decibels higher attenuation in cases where it was exposed to the LoS and low/negative values when the array was in non-line-of-sight (NLoS) conditions during both the LoS and OLoS measurement. The 2-array configuration shows consistent results with the 3- and 4-array system, while it shows to be less affected by blockage. However, note that a 2-array HMD would experience lower mean gain as already shown in Fig. 5.

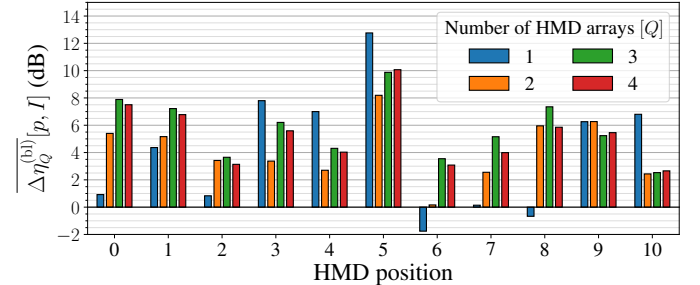


**Fig. 8:** Ratio between mean LoS and OLoS gain. From left to right, the 4 columns at each HMD position represent the 1-, 2-, 3-, and 4-array system.

### D. RMS delay spread and frequency-selective fading

The reception of MPCs and the flatness of the channel's spectrum are assessed in Fig. 9 through the RMS delay spread and frequency-selective fading, respectively. Fig. 9a shows that all array configurations observe a similar RMS delay spread of 2.5–22.5 ns, demonstrating that MPCs, including higher order reflections, can contribute to channel gain. Moreover, the measured RMS delay spread translates to a coherence bandwidth of about 45–400 MHz. In addition to the combined result, Fig. 9a illustrates the measurements for four HMD positions to highlight the inconsistency of a single- and a 2-array system. During OLoS measurements at position HMD<sub>0</sub>, both configurations showed a large RMS delay spread since the OLoS

was no longer their dominant MPC. The other configurations were more biased by the strong LoS component in spite of the obstruction. Similarly, the single-array configuration does not receive the LoS at positions HMD<sub>2</sub> and HMD<sub>4</sub>, while it is strongly influenced by higher order reflections. The single array receives a strong LoS component and few other MPCs at position HMD<sub>5</sub>, resulting in a low RMS delay spread. The 2-array configuration is less influenced by the LoS and more by the MPCs at position HMD<sub>5</sub> due to the orientation of the arrays, yielding a larger RMS delay spread.

Fig. 9b shows that, expectantly, combining the channels from a smaller number of arrays (fewer antennas) results in a less consistent gain across the measured bandwidth. Namely, the single- and 2-array configurations feature noticeably worse performance. From the same examples as in Fig. 9a, we see that higher RMS delay spread measurements are usually reflected in pronounced frequency selectivity. Therefore, the results in Fig. 9 indicate, that there are several MPCs available in the channel in case of OLoS conditions, however, due to the MPCs, the channel can not be considered flat over the measured band and channel equalization needs to be applied.

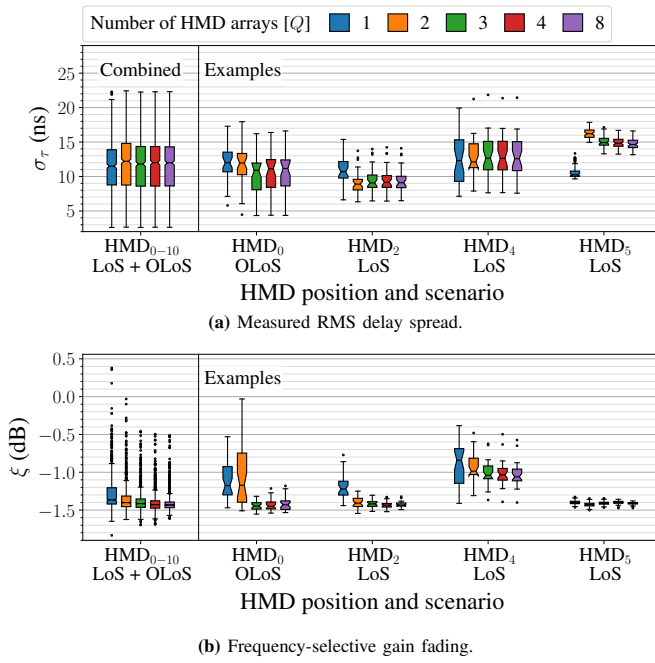


**Fig. 9:** Measured RMS delay spread and frequency-selective fading. Colors represent array configurations. The 8-array results are included for reference.

### E. Spatial multiplexing capability

Fig. 10 shows the mean and minimal service,  $\mathbb{E}[C_Q]$  and  $P_3[C_Q]$ , respectively, at an SNR of 10 dB and for an increasing number of multiplexed streams. These are limited according to  $R_Q = \min(M_Q, N_Q, R_{\text{lim}})$ , where  $R_{\text{lim}}$  is the maximal number of permitted streams. Starting from a single stream and dominant eigenmode transmission (DET), we see that minimal and mean service performance exhibit near-linear growth on the logarithmic scale for spatial multiplexing (SM) and up to 16 streams. The obtained capacity increases with the number of

streams approximately according to  $C \propto R_{\text{lim}}^{0.8}$ . Hence, capacity per stream is highest for DET, and it begins to noticeably decline for more than 16 streams. Furthermore, Fig. 10 shows that the ratio between the minimal service of a single-array and that of a 2-array configuration is larger than their mean service ratio (3.8 versus 1.6). A similar, yet less pronounced, observation can be made for the other configurations.

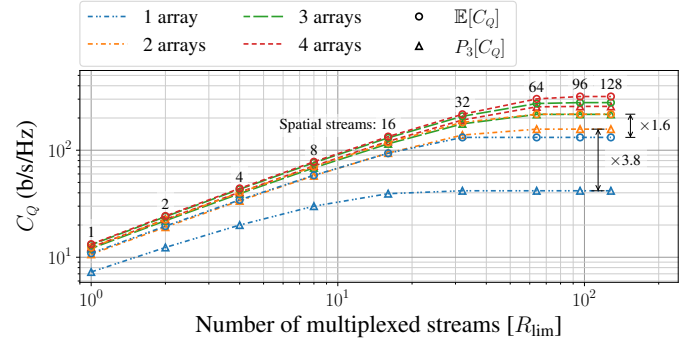


**Fig. 10:** Stream-dependent service performance at an SNR of 10 dB.

Fig. 11 plots the minimal and mean service ratios between 1 and 2, 2 and 3, and 3 and 4 arrays. The procedure is repeated for 1, 32, and 128 spatial streams. These represent DET, the maximal channel rank of the single-array configuration (smallest channel matrix), and the maximal number of available eigenmodes for the 4-array HMD (largest matrix). Recall that the AP features 128 antenna ports, enabling SM on up to 128 streams. In Fig. 11, we can see that adding an antenna array to the HMD yields a significantly more pronounced increase in the minimal service (light shade) than in the mean service (dark shade). Hence, Fig. 11 highlights that evaluating only mean performance can lead to severely underestimating the benefits of employing additional arrays. The performance enhancements are more noticeable for a larger number of eigenmodes, since adding arrays broadens the FoV, which often yields additional MPCs.

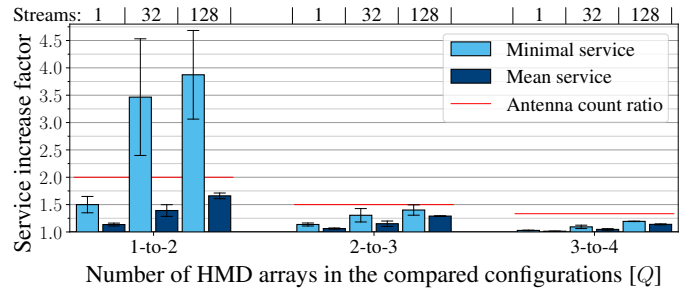
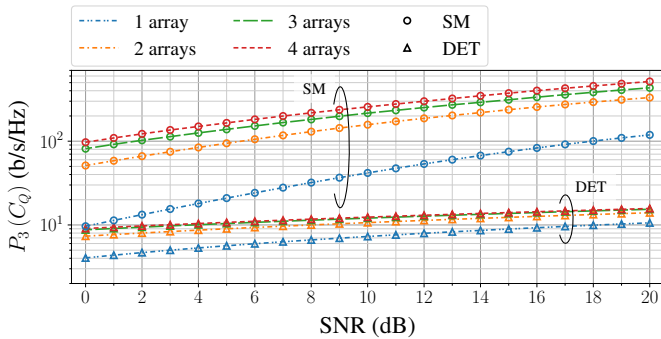


**Fig. 11:** Service improvement due to an additional array, averaged across SNRs 0–20 dB. Vertical confidence intervals represent the standard deviation.

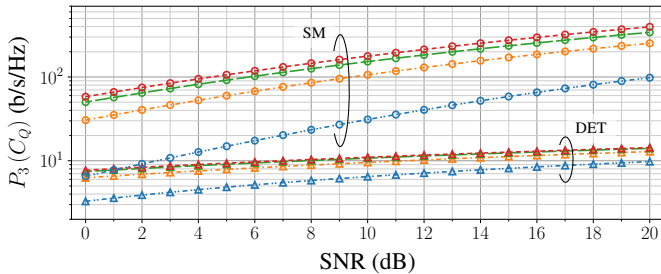
### F. Minimal service

Fig. 12a shows the obtained minimal service ( $P_3[C_Q]$ ) for a 1–4-array configuration, employing either SM or DET and averaging the eigenmode gains across the 768 MHz bandwidth. For DET, we set  $R_Q = 1$  in Equation (11) in order to limit the system to a single eigenmode/stream. Both blue curves confirm

the previous observations, that a single-array HMD is severely affected by rotation. The 2-array configuration improves capacity, however, it still noticeably under-performs when compared to the 3- and 4-array configuration. The latter two offer comparable capacity for DET, while a somewhat larger performance factor separates them for SM. This indicates that a 3-array HMD can capture most of the available signal components, while a fully-digital 4-array MIMO system further enhances performance using the additional multiplexed streams. The dual-polarized 1, 2, 3, and 4 arrays can utilize up to 32, 64, 96, and 128 multiplexed streams, respectively. Fig. 12b shows that the minimal service is lower when calculated per sounding tone, since certain parts of the transmission bandwidth can suffer from fading. Regardless, we observe the same trend as in Fig. 12a – a large gap between a single- and a 2-array configuration, which narrows as a 3<sup>rd</sup> and a 4<sup>th</sup> array is added.



(a) Channel gain first averaged across the transmission bandwidth (768 MHz).



(b) Capacity calculated per sounding tone (375 kHz tone spacing).

**Fig. 12:** Minimal service for SM and DET.

Recall that capacity is calculated for normalized channels and that the evaluated channel matrices consist of 4096–16 384 individual channels. Hence, the relatively high capacity figures. We consider that all configurations have an equal transmit power budget in Fig. 12. Solely from this perspective, the 4-array HMD that utilizes SM is the most energy efficient (lowest energy per transmitted bit). However, powering the additional hardware for each array and utilizing complex baseband processing is likely to reduce energy efficiency in practice. An analysis of the energy efficiency of individual components would be required to reach further conclusions.

## VI. ADDITIONAL DEGREES OF FREEDOM

In this section, we examine the impact of: A. equipping the HMD with a rear headband and mounting an array to it,

B. varying the number of active antennas per HMD antenna array, and C. placing the AP on a wall instead of in the room’s corner. Namely, we evaluate the channel in terms of the six performance metrics and the procedures introduced in Sections IV-B–IV-D. Only the most insightful results are presented.

### A. Utilizing a rear headband

Fig. 13 shows the gain ratio between a forward-facing and a backward-facing  $Q$ -array configuration. The ratios are represented by fitted Gaussian distributions for easier viewing. We notice that a single-array setup facing backward results in a higher average gain (positive mean value in Fig. 13). This means that orienting the array towards the ceiling, rather than the floor, leads to increased gain since the HMD is primarily pitched downward (forward) in our mobility sequence. We attribute the lower gain when pointing towards the floor to the presence of a carpeted and cluttered floor (chair and table legs). Similarly, the 2-array setup favors the backward-facing configuration (arrays at the back and front instead of above the user’s ears), which can be partially attributed to the applied mobility pattern. This pattern benefits the backward-facing configuration when the HMD pitches towards or away from the access point (the pitching motion accounts for approx. 15 out of the total 33 s). On the other hand, a 3-array HMD performs better in the forward-facing configuration (negative mean value in Fig. 13), where two arrays are diagonally positioned at the back and only one array is placed at the front. Hence, the configuration emphasizes MPCs directed towards the ceiling. A 4-array system does not show a preference for either the forward- or backward-facing configuration.

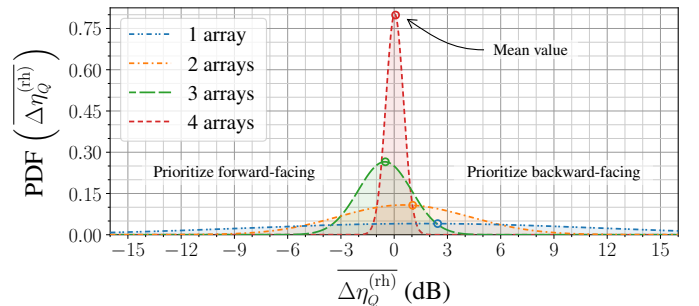


**Fig. 13:** Probability density function (PDF) of the gain ratio between backward- and forward-facing  $Q$ -array configurations.

We expect that the observed biases for the 1–3-array configurations could become less apparent, or even of opposite value, in environments where the floor provides more reflections. Note that the compactness and offset of the probability density functions (PDFs) demonstrate the capabilities of individual array configurations in capturing the available MPCs.

### B. Activating a limited number of antennas in HMD arrays

We have chosen to evaluate the impact of HMD antenna deactivation on the 3-array configuration since it offers a good balance between performance and the number of arrays, as observed in Section V. Fig. 14 shows that activating more antennas results in a gain increase corresponding to the larger

array gain (x-axis), while the gain's distribution becomes more compact as more antennas are activated. The additional antennas increase spatial diversity, lowering the likelihood that a major portion of the channels suffers from fading simultaneously, both across the measured bandwidth (frequency) and across the multiple channel snapshots (time). Correspondingly, activating a larger number of antennas contributes to lower and more compactly distributed frequency-selective fading (y-axis).

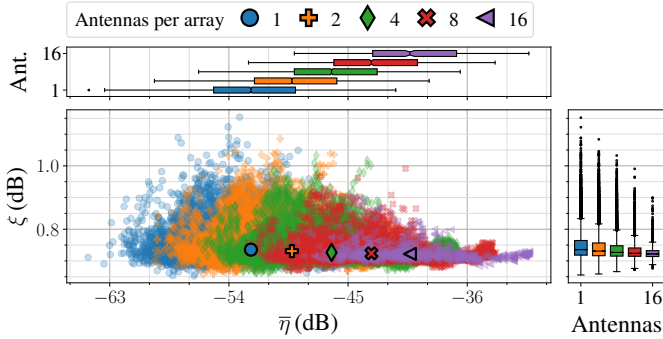


**Fig. 14:** Gain (x-axis) and frequency-selective fading (y-axis) for a 3-array HMD configuration with 1–16 active antennas per array.

Fig. 15 shows that minimal service (capacity's 3<sup>rd</sup> percentile) increases according to the array gain as more antennas are activated. Contrary to the prior evaluation of the number of active antenna arrays in Section V-F, all of the SM curves in Fig. 15 bear a similar shape. This is because a three-array configuration can detect the same MPCs using its (beam-formed) FoV, regardless of the number of active antennas. For example, if three arrays, each with a single active antenna, receive the LoS component, then so will the three arrays with 16 active antennas per array. A larger number of active antennas does, however, increase the beamforming capabilities of the system. The improved spatial filtering enhances SM capabilities, resulting in a consistent capacity gap even as SNR increases. An exception are the DET curves, which start to converge for higher SNRs due to the logarithmic term in calculating capacity and the usage of a single stream.

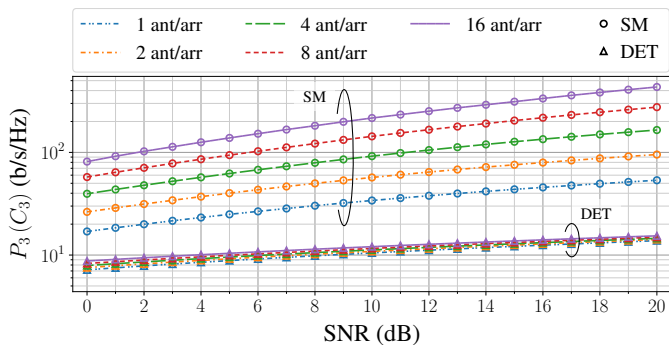


**Fig. 15:** Minimal service for 3-array HMD, 1–16 active antennas per array.

Fig. 16 shows the channel gain correlation when the AP employs either a  $4 \times 4$  (dashed) or a  $4 \times 16$  (solid) array. The former is included to evaluate how correlation might change for smaller AP arrays. For example, due to size and complexity constraints in practical deployments. Fig. 16 confirms that

channel gain correlation decreases with the number of active antennas. Hence, explaining the larger gain spread for configurations with less active antennas in Fig. 14. Furthermore, gain correlation is slightly larger across antennas in the horizontal than in the vertical direction. This happens as each array receives a portion of the available MPCs due to a limited FoV, while, when a high-gain MPC gets reflected from the floor, a table, or the ceiling, a fading dip may occur due to destructive interference. Having a vertical array structure decreases the proportion of antennas that experience this fading dip. The somewhat smaller values of the curve corresponding to a  $4 \times 16$  AP array shows that reducing the likelihood of obtaining low gain due to simultaneous channel fading can be tackled by increasing either the number of HMD or AP antennas.

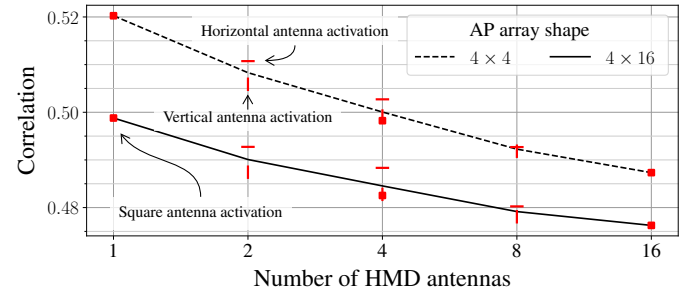


**Fig. 16:** Mean channel gain correlation. Black curves represent the mean correlation across all antenna activation patterns for a given number of active antennas. Red vertical lines, horizontal lines, and squares show the mean correlation for vertical, horizontal, and square activation patterns, respectively.

### C. Impact of AP position and path loss assessment

Fig. 17 illustrates the mean channel gain per HMD position and scenario (LoS/OLoS/combined), and AP deployment. The evaluation utilizes all 8 HMD antenna arrays to provide a holistic view of the available channel gain. We notice that positions HMD<sub>0</sub>, HMD<sub>6</sub>, and HMD<sub>8</sub> show similar gain for both AP<sub>0</sub> and AP<sub>1</sub>, while HMD<sub>4</sub> exhibits higher gain for AP<sub>1</sub>. Gain performance is, on average across the 4 common HMD positions, in favor of AP<sub>1</sub> by -0.3, 1.5, and 0.6 dB for LoS, OLoS, and combined gain, correspondingly.

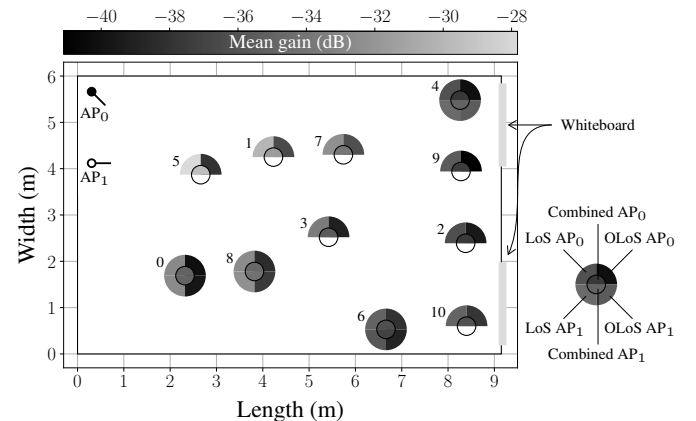


**Fig. 17:** Mean spatial channel gain for both AP deployments. The upper half-circles are reserved for AP<sub>0</sub> and the lower for AP<sub>1</sub>. The left and right side show LoS and OLoS gain, respectively, with the combined gain in the center.



Table IV shows that the higher gain during LoS obstruction at position HMD<sub>4</sub> for AP<sub>1</sub> occurs together with a larger delay ( $\sigma_\tau$ ) and angular spread ( $\sigma_\phi$ ). This can be attributed to additional reflections from the longitudinal wall adjacent to HMD<sub>4</sub> and the whiteboard behind it. The wall-mounted AP shows a slightly higher delay and angular spread on average (last row in Table IV), however, further measurements would be required to conclude on optimal AP deployment strategies. The time delay measurements in Table IV exhibit a high degree of similarity to the reported values by prior art in an office environment and a small meeting room [8, 38]. Namely, the similar room geometry is reflected in similar multipath propagation. Larger indoor environments, especially in OLoS conditions, feature a larger delay and wider angular spread. For instance,  $\sigma_\tau \approx 30$  ns and  $\sigma_\phi \approx 1.5$  in a large lobby [6]. Outdoor scenarios in general feature larger dimensions with less scatterers, resulting in  $\sigma_\tau > 30$  ns and  $\sigma_\phi < 0.5$  [38].

**TABLE IV:** The channel’s mean excess delay ( $\bar{\tau}$ ), RMS delay spread ( $\sigma_\tau$ ), and azimuth spread ( $\sigma_\phi$ ). The final two rows contain the mean results. All of the presented results are derived using the full 8-array configuration.

Position HMD	AP	Measurement – LoS			Measurement – OLoS		
		$\bar{\tau}$ (ns)	$\sigma_\tau$ (ns)	$\sigma_\phi$	$\bar{\tau}$ (ns)	$\sigma_\tau$ (ns)	$\sigma_\phi$
0	0	17.0	7.7	0.42	27.7	14.4	0.71
	1	14.1	8.1	0.31	22.6	9.6	0.50
4	0	30.9	9.2	1.06	33.9	9.5	1.03
	1	33.3	11.6	1.21	36.1	13.7	1.33
6	0	29.6	5.1	0.26	30.3	7.2	0.40
	1	29.0	9.8	0.55	33.3	10.9	0.78
8	0	21.4	9.9	0.46	24.2	10.7	0.65
	1	18.1	7.8	0.36	23.6	9.5	0.44
E	0	24.7	8.0	0.55	29.0	10.4	0.70
	1	23.6	9.3	0.61	28.6	10.9	0.76

Fig. 18 shows the path loss for the entire 8-array configuration (dark shade) and the LoS-oriented array (light shade) at each HMD position. Recall that, at each of the 11 positions, the HMD had a random orientation. At each position, we select the array that is closest to boresight and plot its path loss in light blue. This array receives the largest amount of power from the LoS component among the eight HMD arrays, while MPC reception is limited by its constrained FoV. We see that the LoS-oriented array has a relatively low PLE ( $n = 1.22$ ) compared to prior art, which reports a PLE of  $n = 1.7$ – $1.9$  [6, 10, 38, 39]. We associate this with favorable MPC propagation, including higher order reflections. The MPCs are to a larger extent contained within the room due to the good reflective properties of the whiteboards, metal-coated windows, and concrete walls [41]. The PLE becomes even smaller for the 8-array configuration, which can receive MPCs that impinge the HMD from all azimuth directions. The smaller PLE in the latter case supports the findings on diminishing obstruction severity as distance increases, reported in Section V-C. Similar observations, although with somewhat larger PLEs, were made in [10], where the authors reported  $n = 1.7$  and  $n = 1.2$  for

the so-called directional and omnidirectional PLE, respectively. Note that the vertical difference between the two fitted lines in Fig. 18 represents the gain ratio between a single- and an 8-array configuration in LoS conditions.

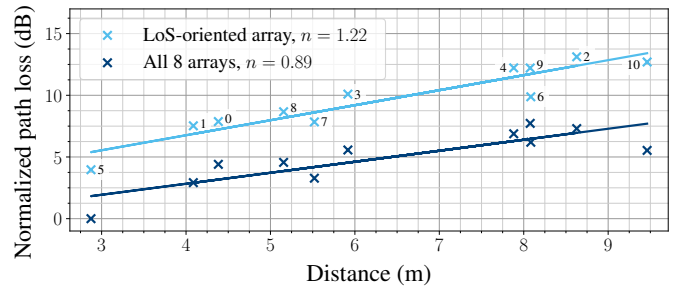


**Fig. 18:** Normalized path loss. The two lines are derived using linear regression with squared error minimization. Light blue and dark blue values are normalized with the same weight in order to preserve the difference between them. Numbers represent HMD positions.

## VII. CONCLUSION

In this work, we studied different mmWave antenna array configurations for HMDs. We introduced six channel performance metrics, analyzed them using analytical models and discussed their application-level significance. Furthermore, the metrics were employed in an empirical evaluation, conducted on 28 GHz MIMO indoor channel sounding data.

The results show that mmWave technology is suitable for high-performance XR applications when the HMD receives the channel’s major MPCs. However, the rotation exhibited by HMD users means that a single-array system will observe unstable channel gain due to its limited azimuth FoV. Distributing additional arrays along the HMD’s azimuth broadens its FoV, allowing for better MPC reception and significantly stabilizing channel gain. Note, however, that the increase in gain is often smaller than suggested by theoretical array gain, since not all of the arrays are equally illuminated by impinging MPCs. Attenuation upon obstruction by a person and its dependency on distance can be roughly predicted by the GTD’s analytical model. Moreover, we noticed that the additional MPCs, received by a multi-array HMD, can lessen the incurred attenuation by several dB. Finally, the reception of additional MPCs can increase orthogonality among the channel’s eigenmodes, enhancing the intrinsic capability of the channel to multiplex spatial streams. The results lead us to the conclusion that it is required to either equip the HMD with multiple arrays or, alternatively, feature macroscopic diversity by employing distributed AP infrastructure. The two can also be considered jointly for high-reliability communication.

With the increased popularity of XR and the pursuit towards wireless HMDs, we can foresee a greater need in emulating physical layer behavior for HMDs. Hence, an prosperous research direction for future work could be to integrate HMD mobility data into channel models. Furthermore, the proposed performance metrics and methodology in this work can be applied to measurement campaigns in other environments, such as city streets and entertainment venues, to further evaluate the behavior of mmWave HMDs in everyday settings.

## ACKNOWLEDGEMENT

Thanks to Meifang Zhu, Gilles Callebaut, and the Lund University volunteers.



This work has received funding from EU programmes Horizon 2020 (No. 861222 – MINTS) and Horizon Europe (No. 101096302 – 6GTandem and No. 101059091 – TALENT), as well as from the Swedish Research Council (No. 2022-04691), ELLIIT, and Ericsson.

## REFERENCES

- [1] F. Firouzi *et al.*, “The Convergence and Interplay of Edge, Fog, and Cloud in the AI-Driven Internet of Things (IoT),” *Information Systems*, vol. 107, p. 101840, 2022.
- [2] M. Shafi *et al.*, “5G: A Tutorial Overview of Standards, Trials, Challenges, Deployment, and Practice,” *IEEE JSAC*, vol. 35, no. 6, pp. 1201–1221, 2017.
- [3] P. Zhou *et al.*, “IEEE 802.11ay-Based mmWave WLANs: Design Challenges and Solutions,” *IEEE Communications Surveys & Tutorials*, vol. 20, no. 3, pp. 1654–1681, 2018.
- [4] X. Cai *et al.*, “Toward 6G with Terahertz Communications: Understanding the Propagation Channels,” *IEEE Commun. Mag.*, to appear, 2024. [Online]. Available: <https://arxiv.org/abs/2209.07864>
- [5] J. Flordelis *et al.*, “Spatial Separation of Closely-Located Users in Measured Massive MIMO Channels,” *IEEE Access*, vol. 6, pp. 40 253–40 266, 2018.
- [6] X. Cai *et al.*, “Dynamic Channel Modeling for Indoor Millimeter-Wave Propagation Channels Based on Measurements,” *IEEE Trans. Commun.*, vol. 68, no. 9, pp. 5878–5891, 2020.
- [7] C. Gustafson *et al.*, “On mm-Wave Multipath Clustering and Channel Modeling,” *IEEE Trans. Antennas Propag.*, vol. 62, no. 3, pp. 1445–1455, 2014.
- [8] X. Wu *et al.*, “60-GHz Millimeter-Wave Channel Measurements and Modeling for Indoor Office Environments,” *IEEE Trans. Antennas Propag.*, vol. 65, no. 4, pp. 1912–1924, 2017.
- [9] J. Huang *et al.*, “Multi-Frequency mmWave Massive MIMO Channel Measurements and Characterization for 5G Wireless Communication Systems,” *IEEE JSAC*, vol. 35, no. 7, pp. 1591–1605, 2017.
- [10] S. Ju *et al.*, “Millimeter Wave and Sub-Terahertz Spatial Statistical Channel Model for an Indoor Office Building,” *IEEE JSAC*, vol. 39, no. 6, pp. 1561–1575, 2021.
- [11] J. Hejselbak *et al.*, “Measured 21.5 GHz Indoor Channels With User-Held Handset Antenna Array,” *IEEE Trans. Antennas Propag.*, vol. 65, no. 12, pp. 6574–6583, 2017.
- [12] S. Aggarwal *et al.*, “A First Look at 802.11ad Performance on a Smartphone,” in *the Proc. of ACM mmNets*, 2019, pp. 13–18.
- [13] K. Zhao *et al.*, “User Body Effect on Phased Array in User Equipment for the 5G mmWave Communication System,” *IEEE Antennas Wireless Propag. Lett.*, vol. 16, pp. 864–867, 2017.
- [14] L. Vähä-Savo *et al.*, “Empirical Evaluation of a 28 GHz Antenna Array on a 5G Mobile Phone Using a Body Phantom,” *IEEE Trans. Antennas Propag.*, 2020.
- [15] B. Xu *et al.*, “Radiation Performance Analysis of 28 GHz Antennas Integrated in 5G Mobile Terminal Housing,” *IEEE Access*, vol. 6, pp. 48 088–48 101, 2018.
- [16] B. Xue *et al.*, “Impacts of Real Hands on 5G Millimeter-Wave Cell-phone Antennas: Measurements and Electromagnetic Models,” *IEEE Trans. Instrum. Meas.*, vol. 72, pp. 1–12, 2023.
- [17] K. Venugopal and R. W. Heath, “Location based performance model for indoor mmWave wearable communication,” in *the Proc. of IEEE ICC*. IEEE, 2016, pp. 1–6.
- [18] R. Gomes *et al.*, “A mmWave Solution to Provide Wireless Augmented Reality in Classrooms,” in *the Proc. of ISWCS*. IEEE, 2018, pp. 1–6.
- [19] J. Struye *et al.*, “Opportunities and Challenges for Virtual Reality Streaming over Millimeter-Wave: An Experimental Analysis,” in *the Proc. of NoF*. IEEE, 2022, pp. 1–5.
- [20] A. Taha *et al.*, “Millimeter Wave MIMO-Based Depth Maps for Wireless Virtual and Augmented Reality,” *IEEE Access*, vol. 9, pp. 48 341–48 363, 2021.
- [21] A. Bedin *et al.*, “DOPAMINE: Doppler frequency and angle of arrival minimization of tracking error for extended reality,” in *the Proc. of ACM CoNEXT*. ACM, 2022, pp. 24–29.
- [22] A. Marinšek *et al.*, “Impact of Array Configuration on Head-Mounted Display Performance at mmWave Bands,” in *2023 EUCNC/6G Summit*. IEEE, 2023, pp. 192–197.
- [23] P. M. Corridon *et al.*, “Does hair impose a significant effect on the propagation of terahertz radiation in human skin?” in *Optical Terahertz Science and Technology*. Optica Publishing Group, 2007, p. MD4.
- [24] X. Cai *et al.*, “A Switched Array Sounder for Dynamic Millimeter-Wave Channel Characterization: Design, Implementation and Measurements,” *IEEE Trans. Antennas Propag.*, submitted, 2023. [Online]. Available: <https://portal.research.lu.se/en/publications/a-switched-array-sounder-for-dynamic-millimeter-wave-channel-char>
- [25] —, “Enhanced Effective Aperture Distribution Function for Characterizing Large-Scale Antenna Arrays,” *IEEE Trans. Antennas Propag.*, vol. 71, no. 8, pp. 6869–6877, 2023.
- [26] C. Gustafson and F. Tuvesson, “Characterization of 60 GHz Shadowing by Human Bodies and Simple Phantoms,” in *the Proc. of EUCAP*. IEEE, 2012, pp. 473–477.
- [27] M. Kunin *et al.*, “Rotation Axes of the Head During Positioning, Head Shaking, and Locomotion,” *Journal of Neurophysiology*, vol. 98, no. 5, pp. 3095–3108, 2007.
- [28] X. Corbillon *et al.*, “360-Degree Video Head Movement Dataset,” in *the Proc. of ACM MMSys*. ACM, 2017, pp. 199–204.
- [29] S. Fremerey *et al.*, “AVtrack360: an open dataset and software recording people’s head rotations watching 360° videos on an HMD,” in *the Proc. of ACM MMSys*. ACM, 2018, pp. 403–408.
- [30] S. Blandino *et al.*, “Head Rotation Model for Virtual Reality System Level Simulations,” in *the Proc. of IEEE ISM*. IEEE, 2021, pp. 43–49.
- [31] F. Bellili *et al.*, “On the lower performance bounds for doa estimators from linearly-modulated signals,” in *the Proc. of BSC*. IEEE, 2010, pp. 381–386.
- [32] G. L. James, *Geometrical Theory of Diffraction for Electromagnetic Diffraction*. Peter Peregrinus, London, UK, 1986.
- [33] A. F. Molisch, *Wireless Communications*, 3rd ed. Wiley Publishing, New Jersey, US, 2022, p. 398.
- [34] T. L. Marzetta *et al.*, *Fundamentals of Massive MIMO*. Cambridge University Press, Cambridge, United Kingdom, 2003.
- [35] J. Nightingale *et al.*, “Subjective Evaluation of the Effects of Packet Loss on HEVC Encoded Video Streams,” in *the Proc. of ICCE*. IEEE, 2013, pp. 358–359.
- [36] D. H. Morais, *5G NR, Wi-Fi 6, and Bluetooth LE 5: A Primer on Smartphone Wireless Technologies*. Springer Nature, Cham, Switzerland, 2023.
- [37] A. Paulraj *et al.*, *Introduction to Space-Time Wireless Communications*. Cambridge University Press, Cambridge, United Kingdom, 2003.
- [38] H. Xu *et al.*, “Spatial and temporal characteristics of 60-GHz indoor channels,” *IEEE JSAC*, vol. 20, no. 3, pp. 620–630, 2002.
- [39] K. Haneda *et al.*, “Indoor 5G 3GPP-like channel models for office and shopping mall environments,” in *the Proc. of IEEE ICC*. IEEE, 2016, pp. 694–699.
- [40] R. McGill *et al.*, “Variations of box plots,” *The American Statistician*, vol. 32, no. 1, pp. 12–16, 1978.
- [41] H. Zhao *et al.*, “28 ghz millimeter wave cellular communication measurements for reflection and penetration loss in and around buildings in new york city,” in *the Proc. of IEEE ICC*, 2013, pp. 5163–5167.



**Alex Marinšek** (Student Member, IEEE) is a doctoral student at the DRAMCO lab at KU Leuven and part of the MINTS MSCA-ITN project, where he specializes in mmWave wireless communication for XR use cases. He received his M.Sc. degree in Electrical Engineering from the University of Ljubljana, Slovenia, where he was also a recipient of the national Zois scholarship. During his studies, he has authored and co-authored several scientific publications and designed an award-winning learning activity at the European Union's Science is Wonderful! 2023 competition.



**Xuesong Cai** (Senior Member, IEEE) received the B.S. degree and the Ph.D. degree (with distinction) from Tongji University, Shanghai, China, in 2013 and 2018, respectively. In 2015, he conducted a three-month internship with Huawei Technologies, Shanghai, China. He was also a Visiting Scholar with Universidad Politécnica de Madrid, Madrid, Spain in 2016. From 2018-2022, he conducted several postdoctoral stays at Aalborg University and Nokia Bell Labs, Denmark, and Lund University, Sweden. He is currently an Assistant Professor in Communications Engineering and a Marie

Skłodowska-Curie Fellow at Lund University, closely cooperating with Ericsson and Sony. His research interests include radio propagation, high-resolution parameter estimation, over-the-air testing, resource optimization, and radio-based localization for 5G/B5G wireless systems. His work has led to over 64 peer-reviewed publications, 2 book chapters, and 4 granted patents.

Dr. Cai was a recipient of the China National Scholarship (the highest honor for Ph.D. Candidates) in 2016, the Outstanding Doctorate Graduate awarded by the Shanghai Municipal Education Commission in 2018, the Marie Skłodowska-Curie Actions (MSCA) "Seal of Excellence" in 2019, the EU MSCA Fellowship (ranking top 1.2%, overall success rate 14%) and the Starting Grant (success rate 12%) funded by the Swedish Research Council in 2022. He was also selected by the "ZTE Blue Sword-Future Leaders Plan" in 2018 and the "Huawei Genius Youth Program" in 2021. He is an AP-S 2024 Young Professional Ambassador and serves as an Editor of IEEE Transactions on Vehicular Technology, IET Communications, and Wireless Communications and Mobile Computing.



**Lieven De Strycker** (Member, IEEE) is a full professor at the Faculty of Engineering Technology, Department of Electrical Engineering, KU Leuven. He was a coordinator of European Erasmus Intensive teaching programs (Life Long Learning program). Prof. L De Strycker was an invited speaker on indoor localization at several universities (Darmstadt, Porto, Iasi, Plovdiv, Suceava, La Rochelle). In 2001 he joined the Engineering Technology department of the Catholic University College Ghent (KAHO Sint-Lieven), where he founded the DRAMCO (wireless and mobile communications) research group in cooperation with

ESAT-TELEMIC, KU Leuven. He is still the coordinator of the DRAMCO research group which has been involved in over 20 national and international research projects. He did an IAESTE traineeship at Siemens Madrid, Spain. He did research in European FP5 and national R&D projects at the INTEC\_design Lab of Prof. Jan Vandeweghe and received the Ph.D. degree in Electrotechnical Engineering from Gent University in 2001 (summa cum laude). His Master degree in Electrotechnical Engineering he received at Ghent University, in 1996 (summa cum laude).



**Fredrik Tufvesson** (Fellow, IEEE) received his Ph.D. in 2000 from Lund University in Sweden. After two years at a startup company, he joined the department of Electrical and Information Technology at Lund University, where he is now professor of radio systems. His main research interest is the interplay between the radio channel and the rest of the communication system with various applications in 5G/B5G systems such as massive MIMO, mm wave communication, vehicular communication and radio-based positioning. Fredrik has authored around 110 journal papers and 175 conference papers, he is fellow of the IEEE and his

research has been awarded with the Neal Shepherd Memorial Award (2015) for the best propagation paper in IEEE Transactions on Vehicular Technology, the IEEE Communications Society best tutorial paper award (2018, 2021) and the IEEE Signal Proc. Society Donald G. Fink overview paper award 2023.



**Liesbet Van der Perre** (Senior Member, IEEE) received the M.Sc. and Ph.D degree in Electrical Engineering from the KU Leuven, Belgium, in 1992 and 1997 respectively. Dr. Van der Perre joined imec's wireless group in 1997 and took up responsibilities as senior researcher, system architect, project leader and program director, until 2015. She was appointed full Professor in the DRAMCO lab of the Electrical Engineering Department of the KU Leuven and guest professor at the University of Lund in 1996. Her main research interest is in energy efficient wireless connectivity

and embedded systems, with applications in multiple antenna and large array systems, IoT and broadband networks.